Friction

Research Article

Effect of hydrostatic pressure on the tribological behavior and mechanism of the multilayered graphite like-carbon (GLC) coating

Yingrui Liu[1,2,3], Xiaohui Zhou[1,4], Peng Guo[1], Yinshui Liu[6], Jing Wei[1], Wei Yang[1], Kazuhito Nishimura[1], Aiying Wang[1,5], Peiling Ke[1,5]✉

Cite this article: Liu Y, Zhou X, Guo P, et al. *Friction* 2025, **13**: 9440958. https://doi.org/10.26599/FRICT.2025.9440958

ABSTRACT: In this study, the tribological behavior and mechanism of multilayered graphite-like carbon (GLC) coatings under different hydrostatic pressures (0.1–60 MPa) were investigated via a simulated deep-sea friction and wear test system. The morphology and composition of the friction interface were thoroughly characterized. The findings revealed that the coefficient of friction (COF) was greater (but did not surpass 0.02) under conditions of elevated hydrostatic pressure or heavy load. The GLC coating mainly experiences abrasive wear, and the degree of wear intensifies with increasing hydrostatic pressure and load. The graphitization of the friction interface and the production of silicon-based lubrication products are becoming increasingly evident. Consequently, the effect of hydrostatic pressure on the frictional performance of GLC coatings is achieved by changing the state of the frictional contact surfaces. Essentially, hydrostatic pressure modifies the real contact area of the friction pair by generating additional compressive loads such that an increase in hydrostatic pressure has a similar effect on an increase in the applied load. As the hydrostatic pressure and applied load increase, the trend of abrasion smoothing on the surfaces of the friction pair becomes more pronounced. The graphite transfer film and silicon-based material generated during the friction process improve the lubrication performance of the friction pair, resulting in extremely low wear of the friction pair.

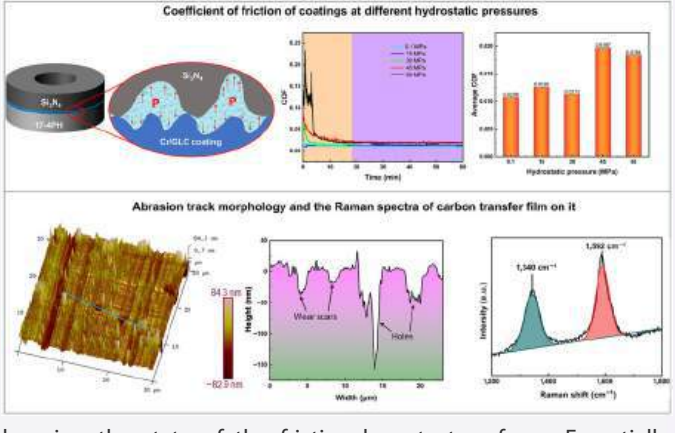

KEYWORDS: graphite-like carbon (GLC) coating; deep sea; friction; contact pressure

1 Introduction

The development of marine resources is inseparable from the support of advanced marine equipment and materials. In seawater reciprocating pumps, for example, it is essential to protect the surfaces of friction pairs such as pistons/cylinders, shoes/discs, and water-lubricated bearings, which often suffer severe damage from both seawater corrosion and wear. Applying surface protective coatings can effectively prolong the service life of moving components. Metal nitride hard coatings (TiN and CrN) and amorphous carbon coatings are two extensively researched types of anti-tribocorrosion coating materials. Compared with metallic nitride coatings, amorphous carbon coatings exhibit excellent chemical stability, increased hardness, and inherent self-lubricating properties, making them superior choices for wear-resistant coatings in marine environments. Graphite-like carbon (GLC) coatings, as typical amorphous carbon coatings, are characterized by a significant proportion of sp^2-hybridized carbon, and the absence of hydrogen in GLC coatings leads to weak attraction for water molecule adsorption [1, 2]. As a result, the

[1] Key Laboratory of Marine Materials and Related Technologies, Zhejiang Key Laboratory of Marine Materials and Protective Technologies, Ningbo Institute of Materials Technology and Engineering, Chinese Academy of Sciences, Ningbo 315201, China. [2] Chongqing Institute of Green and Intelligent Technology, Chinese Academy of Sciences, Chongqing 400714, China. [3] Chongqing Institution of Bio-intelligent Manufacturing, Chongqing 401120, China. [4] School of Physical Science and Technology, ShanghaiTech University, Shanghai 201210, China. [5] Center of Materials Science and Optoelectronics Engineering, University of Chinese Academy of Sciences, Beijing 100049, China. [6] State Key Laboratory of Digital Manufacturing Equipment and Technology, School of Mechanical Science and Engineering, Huazhong University of Science and Technology, Wuhan 430074, China.

✉ Corresponding author. E-mail: kepl@nimte.ac.cn

Received: January 27, 2024; Revised: May 31, 2024; Accepted: June 30, 2024

environmental sensitivity of the coating is significantly reduced [3, 4], producing stable and exceptional low-friction lubrication features under aqueous lubricating conditions, making GLC an optimal choice for surface protective coatings on mobile components in marine settings [5]. A lot of research has been carried out on the tribological properties of GLC coatings in ambient environments, with a particular emphasis on comparing and explaining the tribological performance under different friction conditions [5–7], and significant progress has been made in this area [8, 9]. Furthermore, to enhance the load-bearing capacity of GLC coatings, numerous methods have been employed, including optimization of deposition parameters [10, 11], element doping [12, 13], multilayered structure design [14], and gradient structure design [15]. Coatings fabricated with these approaches have been systematically investigated for their tribological performance under water-lubricated conditions. Previous research has indicated that the tribological failure of GLC coatings in water-lubricated environments is closely associated with microstructural defects formed during the coating deposition process. In corrosive environments, corrosive solutions can infiltrate the coating/substrate interface through inherent defects of coatings, such as pores or wear-induced pits and cracks, which serve as corrosion pathways [16]. Near these pathways, a galvanic cell forms between the coating, substrate, and seawater medium, leading to electrochemical reactions. In the presence of coupled sliding and corrosion, coating failure is accelerated, resulting in interface cracking or coating delamination [17]. Therefore, improving densification of coatings is a crucial strategy for extending their service life.

Owing to the elevated hydrostatic pressure in deep-sea environments, the distribution of contact stress and the lubrication properties of water at the contact surfaces of friction pairs undergo significant alterations. Consequently, this leads to variations in the tribological behavior of these friction pairs. Several studies have shown that the tribological behavior of materials in high hydrostatic pressure environments is significantly different from that in atmospheric conditions. For example, Wang et al. [18, 19] observed that the wear rate of bulk metals, such as 316L stainless steel, Hastelloy, and nickel-based high-temperature alloys, increased with increasing hydrostatic pressure when they were in self-mated conditions. In contrast, the wear rate of Ti6Al4V decreased rapidly as the hydrostatic pressure increased. The authors attributed this varying wear rate trend with depth to the competitive effects of seawater's "wedging action" and lubrication. In the case of thermoplastic polymers such as polytetrafluoroethylene (PTFE), which are used as lubricants, Liu et al. [20, 21] found that high hydrostatic pressure significantly promoted the migration and diffusion of seawater into PTFE and its composites. This considerably amplifies the material's water absorption, leading to the refinement and localized degradation of polymer grains, which causes a reduction in the material's mechanical strength. Ultimately, this results in increased wear in polymer materials under high hydrostatic pressure conditions in deep-sea environments. For protective coating materials, Wu et al. [22] discovered that hydrostatic pressure did not enhance the tribological properties of thermal-sprayed WC–10Co–4Cr coatings and Si_3N_4. Nonetheless, increasing the load under certain hydrostatic pressure conditions resulted in lower friction coefficients and wear rates. This illustrated that the wear mechanisms in atmospheric environments may not fully elucidate their behavior under deep-sea conditions. Therefore, to facilitate the design and selection of materials for friction pairs in high hydrostatic pressure environments, a thorough examination of material tribological behavior is crucial.

Although GLCs exhibited both high corrosion resistance under high hydrostatic pressure of up to 30 MPa [23, 24] and long-term tribocorrosion resistance of up to 1,728 m in a 3.5 wt% NaCl solution [25], there is currently no available research regarding their anti-tribocorrosion performance under high hydrostatic pressure conditions. Hence, this study selected a typical Cr/GLC multilayered coating and employed a simulated deep-sea environmental tribological and corrosion testing apparatus to systematically investigate the impact of hydrostatic pressure and contact pressure on the tribological behavior of the carbon-based coating. This study aims to elucidate the tribological behavior of the GLC coating system in hydrostatic pressure environments, providing a foundation for further optimization and fabrication of GLC coatings applied under deep-sea conditions.

2 Experimental

2.1 Experimental materials

The selection of 17-4PH precipitation hardening stainless steel as the base material is based on its high strength, high hardness and excellent corrosion resistance properties. This stainless steel is widely used in marine applications, particularly for shaft components. A Cr/GLC multilayered coating is deposited on its surface to act as a friction ring. Sintered Si_3N_4 ceramic rings were selected as the counterparts. The Si_3N_4 ceramic displays remarkably high hardness (1,628±100 $HV_{0.3}$) and outstanding corrosion resistance [26]. The Si_3N_4 ceramic friction ring has a porosity of 1%, a density of 3.2 g/cm^3, and a surface roughness of less than 60 nm. As a friction pairing material, it is virtually impervious to water, making it appropriate for underwater friction applications. The Cr/GLC multilayered coatings were deposited with direct current magnetron sputtering (DCMS) using an alternate method. The detailed fabrication procedure of these typical GLC coatings has been described in our previous studies, and detailed information can be found in Refs. [16, 17]. The friction pair consisted of two identical friction rings, and the experiments were conducted in rotational friction mode. Both friction rings are ring shaped. The upper friction ring is made up of sintered Si_3N_4 ceramics, while the friction ring below is composed of 17-4PH stainless steel with Cr/GLC multilayered coating deposited on the surface. The thickness of both friction rings is 8 mm, and the dimensions of the friction contact area are as follows: inner diameter φ24 mm and outer diameter φ30 mm, resulting in a calculated contact area of 2.54×10^{-4} m^2 for the friction pair. The dimensions of the friction specimens and the mating arrangement are illustrated in Fig. 1.

2.2 Friction experiment

The tribological experiments were carried out using a simulated deep-sea friction-corrosion test machine. Detailed information on this friction machine can be found in Refs. [27, 28]. This study focuses on two key factors affecting tribological performance: hydrostatic pressure and contact load. Specifically, when the load was fixed at 500 N, the influence of different hydrostatic pressures (0.1, 15, 30, 45, and 60 MPa, with accuracy of 1 MPa) on the tribological behavior of the friction pair was investigated. When the hydrostatic pressure was fixed at 15 MPa, the effect of applied load (500, 1,000, and 1,500 N) on the tribological behavior of the friction pair was investigated. A 3.5 wt% NaCl solution was used as the medium during the experimental process. The specific experimental procedure is as follows:

(1) When the study variable is hydrostatic pressure, the output pressures of the hydraulic pump of the friction test machine are

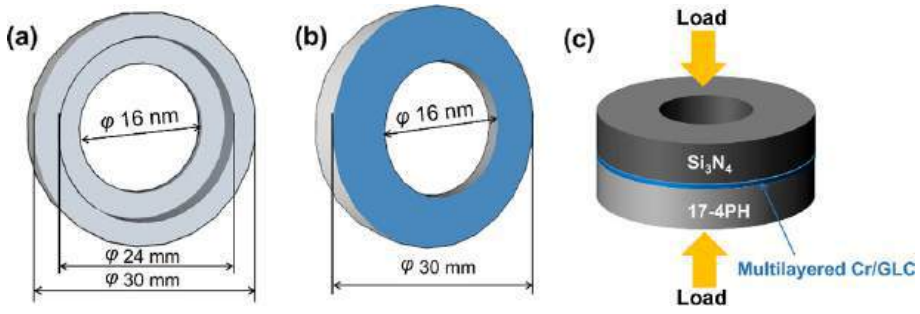

Fig. 1 Schematic of friction rings: (a) Si_3N_4 ceramic friction ring, (b) 17-4PH friction ring with Cr/GLC multilayered coating deposited on the surface, and (c) assembly diagram of friction rings.

set to 0.1, 15, 30, 45, and 60 MPa. The hydraulic oil pump is set to output a constant load force of 500 N (with accuracy of 2 N). Based on the contact area of the friction pair, the contact stress at the friction interface can be calculated as 1.96 MPa.

(2) When the study variable is the load, the output hydrostatic pressure of the multi-plunger hydraulic pump is set to 15 MPa (with accuracy of 1 MPa), and the hydraulic oil pump is set to output load forces of 500, 1,000, and 1,500 N, respectively. At this point, the corresponding contact stresses between the friction pairs are 1.96, 2.92, and 5.88 MPa.

(3) The rotational speed of the friction pair is set to 1,000 r/min, resulting in a relative sliding linear velocity of 1.36 m/s for testing the friction ring.

The duration of all friction experiments was 1 h, and each test was repeated in three separate experiments.

2.3 Characterization and analysis

Coating morphology before and after tribological experiments was observed and analyzed using a field emission scanning electron microscope (FE-SEM; Quanta 250, FEI Company, USA). For detailed observation of surface defects, ion beam cutting was performed using a focused ion beam scanning electron microscope (FIB-SEM; Auriga, Germany), followed by analysis of morphological characteristics and material types in the wear area using the equipped energy dispersive X-ray spectroscopy (EDS) probe. Raman spectroscopy (Renishaw-inVia reflex, UK) with an excitation light source at 532 nm was applied to characterize the carbon bond structure of the surface of the friction pair before and after the tribological experiments. A scanning probe microscope (Dimension 3100V, Veeco, USA) was used to characterize the three-dimensional surface morphology features of the friction pair surface. The tests were carried out in a tapping mode on a selected 30 μm × 30 μm square area using a Si_3N_4 probe with a tip radius of 8 nm.

3 Results

3.1 Surface morphologies of friction pairs

The structural and morphological characteristics of the friction pairing surface have a direct influence on the friction contact mode. Analyzing the morphology and structural features of the friction pair surface of the as-deposited coating is crucial for understanding the friction mechanisms under different conditions. Figure 2 shows the surface morphology of Cr/GLC multilayered coatings and structural diagrams of two types of growth defects. Figure 2(a) reveals that the entire surface of the coating is very smooth and flat at low magnification, with no apparent cracks or protrusions. The high-magnification inset in the upper right corner shows that the surface of the film has cauliflower-like clustering features. This is caused by the epitaxial growth of the top GLC layer on the columnar crystalline surface of the Cr transition layer and its island-like growth process [29, 30]. Since the performance of GLC coatings in the friction process is not only related to the tribological test conditions but also directly affected by the growth defects that form during the coating growth process, further analysis of the growth defects on the coating surface is necessary [31].

The structural and compositional results of two typical types of nodular and penetrating defects are shown in Fig. 2(b). Figures 2(c) and 2(d) show the two cross-sectional structures of nodular defects, which formed at the middle and bottom of the Cr/GLC multilayered coating. The total thickness of the coating is approximately 2.1 mm. Obviously, these protruding nodular defects result from the local adsorption and deposition of inclusions during the alternate deposition process. In addition, there are noticeable cracks around the defects, which can lead to weak adhesion strength to the substrate. Under the influence of subsequent friction or other external forces, these defects can delaminate and eventually form crater-like or penetrating defects. Figure 2(c) illustrates a localized elevation on the top layer of the coating, resulting from carbon particle adsorption (as indicated in the spectrum depicted in Fig. 2(e)). Figure 2(d) clearly shows that these particles commence adsorption in the initial layer of the coating. With periodic alternate deposition, they eventually culminate in localized elevations at the top layer. As a result, this type of protruding nodular defect is more widely distributed within the coating and affects the performance of the coating. Studies of the effects of coating defects on friction performance have shown that in nitride-based coatings produced by physical vapor deposition (PVD) techniques, protuberant nodular defects often become stress concentration points during the friction process. When these protruding nodular defects detach, they can transform into hard particles between friction pairs, resulting in severe three-body wear and significantly accelerating coating wear and failure [32–34].

Figure 3 displays the surface morphology and EDS mapping results of the Si_3N_4 friction ring. It appears relatively even in structure, with an even distribution of elements. Nonetheless, production and processing of Si_3N_4 produce several defects, such as cracks, pits, and scratches. The magnified images in Figs. 3(c) and 3(d) depict the prevalent surface defects found in Si_3N_4, referred to as pitting. Pitting arises from the creation of sharp protrusions by abrasive particles during the polishing process, which causes lateral cracks in the subsurface. These transverse cracks then propagate to the surface to form pits [35]. Figure 4 shows the three-dimensional (3D) morphology and cross-sectional profiles of the multilayered Cr/GLC coating and Si_3N_4 ring surface. The blue lines on the cross-sectional profiles depict the distribution of depth in a specified direction. As shown in

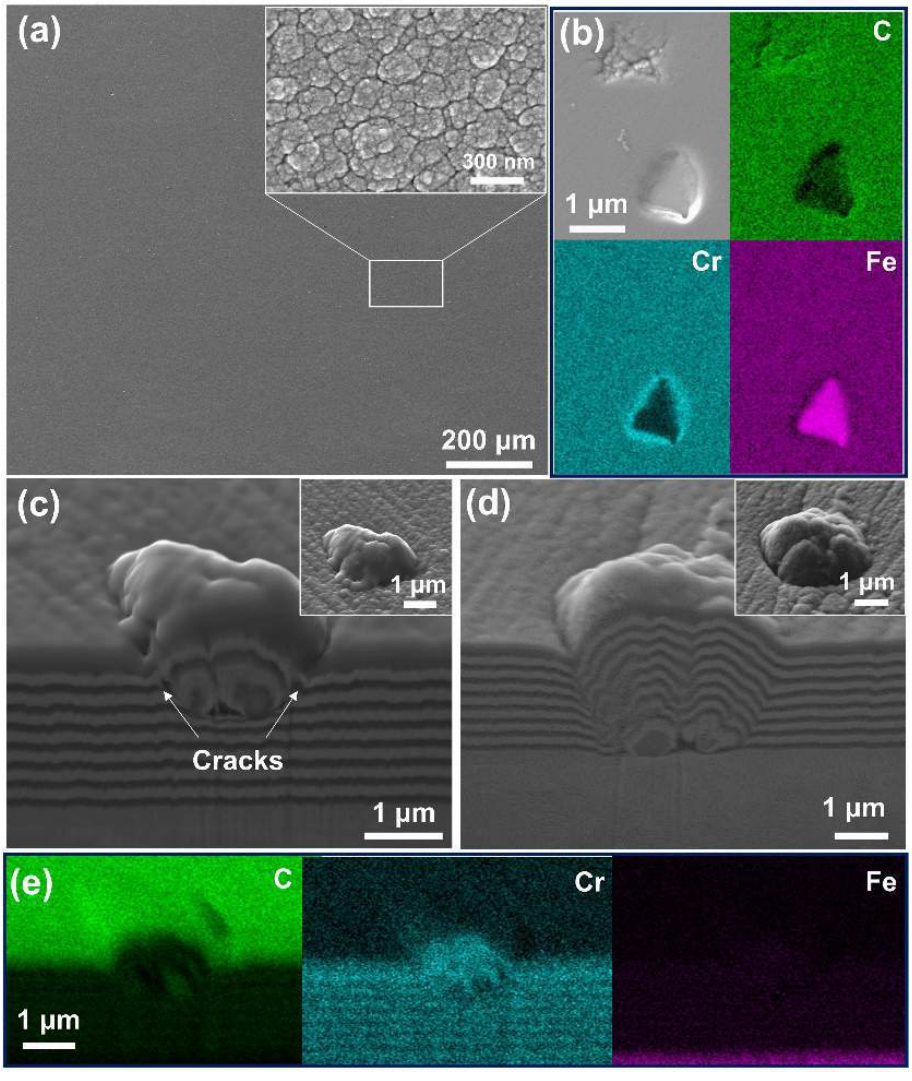

Fig. 2 (a) Surface morphology of as-deposited Cr/GLC multilayered coating; (b) nodular-like and penetrating growth defects and corresponding EDS mapping results; (c) two types of nodular-like defects and (d) corresponding EDS mapping results.

Figs. 4(a)–4(c), the surface of the multilayered Cr/GLC coating shows typical periodic undulations, which are a manifestation of the cauliflower-like cluster growth of the top GLC layer. Within the tested region, the entire surface of the coating appears to be smooth and free of any discernible defect, with a roughness of only 6.98 nm. The surface morphology and cross-sectional profiles of the Si_3N_4 ring ceramics are depicted in Figs. 4(b)–4(d). The whole examined area displays local undulations characterized by depressions and protrusions. The maximum depth of surface pit defects, as evidenced by the cross-sectional profiles, reaches 80 nm. Owing to surface irregularities and pit defects, the roughness of Si_3N_4 ceramics ring is greater than that of the multilayered Cr/GLC coating, which measures 14.6 nm.

3.2 Tribological property analysis

3.2.1 Tribological behavior of friction pairs under different hydrostatic pressures

Figure 5 shows the friction curves of the Cr/GLC–$S_{i3}N_4$ friction pair under a constant load of 500 N at different hydrostatic pressures. During the test duration, the trends of the friction curves under different hydrostatic pressure conditions are similar, as shown in Fig. 5(a). However, distinctions in duration and characteristics of the initial running-in phase are observed under these different conditions. Therefore, a phase analysis of these friction curves was carried out. Figure 5(b) illustrates the initial running-in phase. Although there are some fluctuations, the curves remain relatively smooth until the hydrostatic pressure reaches 60 MPa, at which point the initial friction coefficient reaches its maximum. These fluctuations become more pronounced and spike-like within the first 4 min. After a magnified analysis of a spike (as illustrated in the inset), it is apparent that it lasted for approximately 4 s, with a slow increase and quick decrease. An analysis of the surface morphology characteristics of the friction pair suggested that this abrupt spike may be related to changes in the lubricating state of the friction surface and changes in the interfacial structure.

The time it takes for the friction curve to enter the stable phase is also influenced by the hydrostatic pressure. A running-in phase is virtually absent in the friction curve when the hydrostatic pressure is less than 15 MPa. However, as the hydrostatic pressure increases, the duration of the running-in period gradually increases. For example, the friction curve takes approximately 4 min to enter the stable phase at a hydrostatic pressure of 60 MPa.

Figure 5(c) illustrates the friction curves acquired during the last 20 min of friction experiments. If the hydrostatic pressure

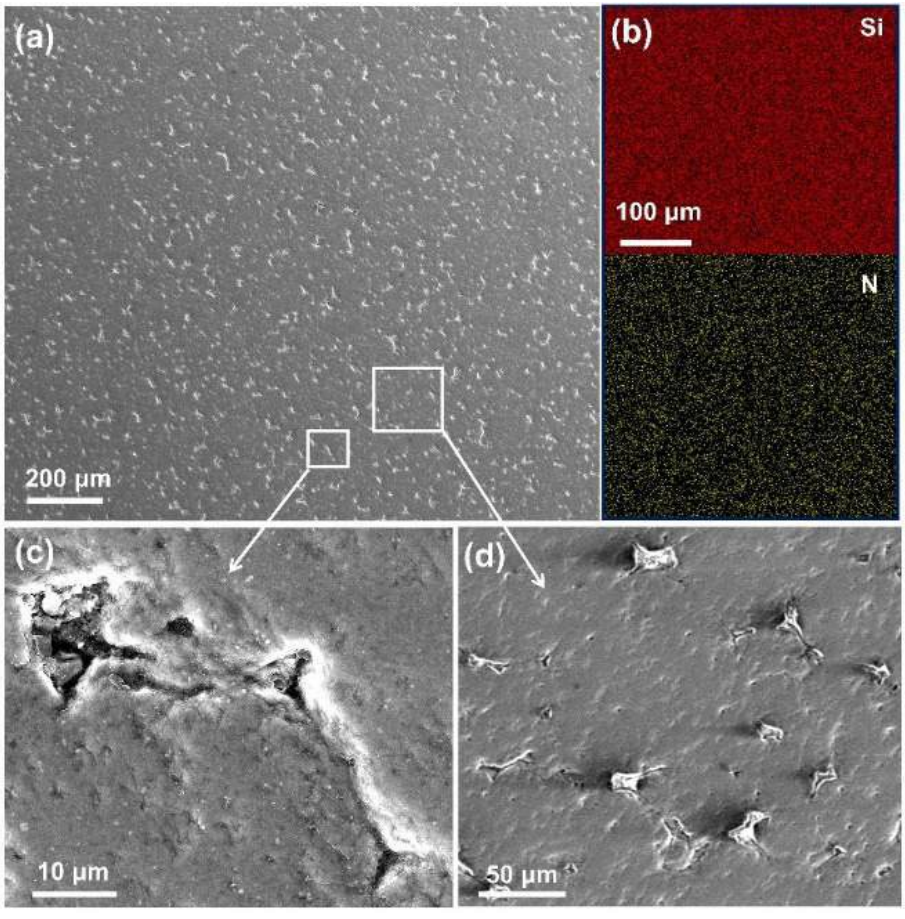

Fig. 3 Surface morphology and EDS mapping results of Si_3N_4 friction ring.

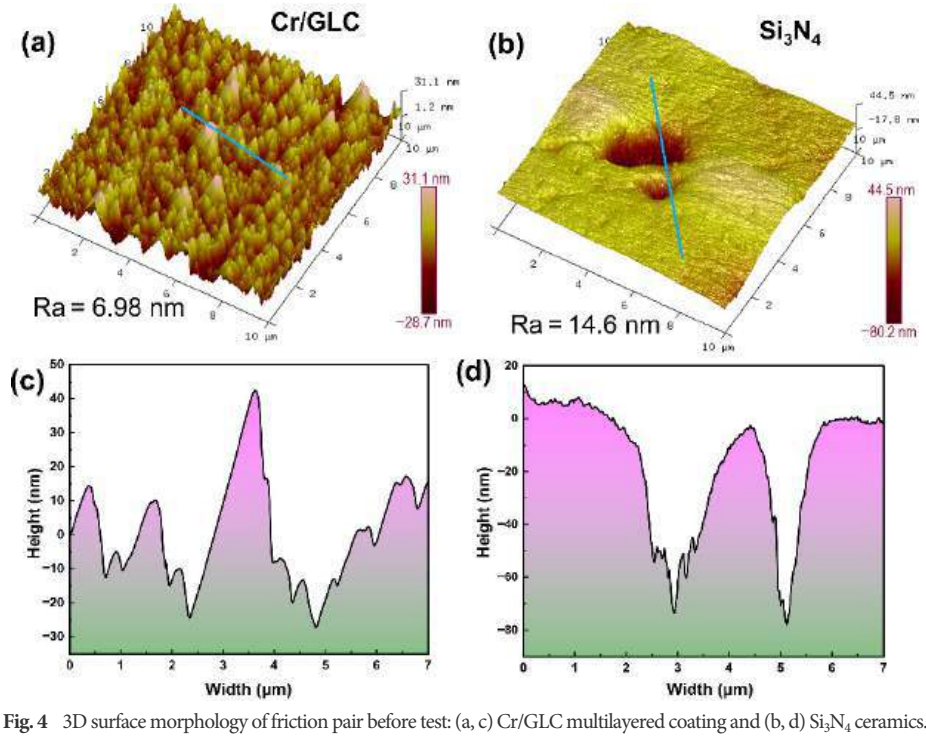

Fig. 4 3D surface morphology of friction pair before test: (a, c) Cr/GLC multilayered coating and (b, d) Si_3N_4 ceramics.

stays at 30 MPa, the friction curves exhibit fewer sudden and sharp peaks and remain quite stable and smooth. Notably, when the pressure is 0.1 MPa (atmospheric pressure), the friction curve has the lowest coefficient of friction (COF) at 0.006. In contrast, when the hydrostatic pressure exceeds 30 MPa, there is an increase in the occurrence of spikes and abrupt changes in the friction curves. These changes are attributed to alterations in the surface state of the friction pair. Figure 5(d) presents the average

coefficient of friction calculated during the test period under the respective hydrostatic pressure test conditions. When the hydrostatic pressure is less than 30 MPa, the average COFs are almost identical (COF ≈ 0.01) and show minimal variation. Once the hydrostatic pressure exceeds 30 MPa, the coefficient of friction increases significantly, peaking at 0.0197 at 45 MPa, which is the highest value among all the experimental conditions. The hydrostatic pressure therefore has a significant effect on the initial interfacial lubrication state of the friction pair, resulting in marked variations in the friction curves. Additionally, the hydrostatic pressure leads to unstable friction curves and increased COFs. There is no clear positive correlation between the hydrostatic pressure and alterations in COFs. The variations in interface lubrication states under different testing conditions might be responsible for this outcome.

3.2.2 Tribological behavior of friction pairs under different applied load forces

Figure 6 shows the friction curves under different load conditions at a hydrostatic pressure of 30 MPa. The friction curves display significant fluctuations during the initial run-in period as the applied load increases from 500 to 1,500 N, with the most prominent fluctuations appearing at 1,500 N. As the friction time increases, the friction curves gradually decrease and gradually remain in a stable phase. Throughout the period of testing, all the friction curves display a consistent trend of initially decreasing from one stable state to a lower stable state, indicating a gradual improvement in the lubrication state of the friction interface as the friction time increases. The average COFs obtained during the final 20 min of the stable phase are depicted in Fig. 6(b), and they gradually increase as the load increases. The deterioration of the lubrication state at the friction interface may be responsible for the increased COFs due to higher loads. Further discussion on the friction interface is provided below.

3.3 Wear morphology analysis

3.3.1 Wear morphologies under different hydrostatic pressures

Figure 7 shows the friction surface morphology and cross-sectional profile of Cr/GLC multilayered coatings under different

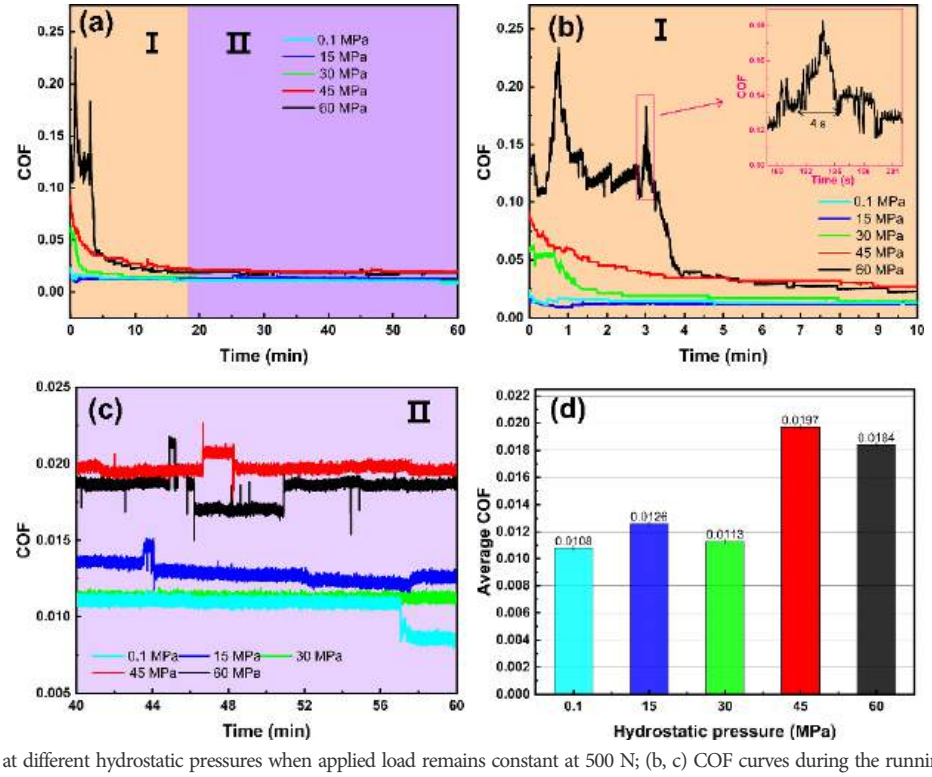

Fig. 5 (a) COF curves at different hydrostatic pressures when applied load remains constant at 500 N; (b, c) COF curves during the running-in and stable periods; (d) average COFs.

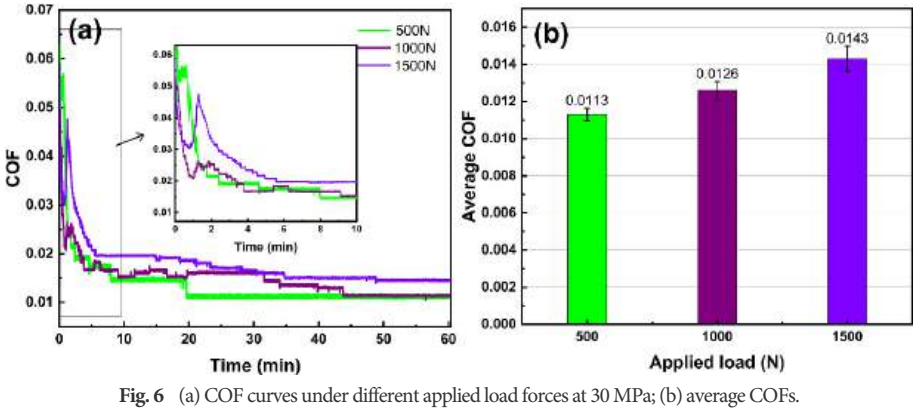

Fig. 6 (a) COF curves under different applied load forces at 30 MPa; (b) average COFs.

hydrostatic pressures with a constant load of 500 N. Notably, it can be seen from the surface wear crack (Figs. 7(a)–7(c)) that there is no evidence of coating delamination after the friction test, which can be attributed to the relatively low surface contact stress (1.96 MPa). All samples display parallel furrows on the surface of friction, oriented parallel to the direction of rotation, indicating that abrasive wear dominates the wear mechanism. Notably, the furrows on the surface of all the samples are unevenly distributed, suggesting that the friction contact during the process is not characterized merely by face-face contact. Residual NaCl has been identified as white substances on the friction surface, indicating the coexistence of water lubricated and solid–solid contact regions along the entirety of the frictional contact interface.

The 3D surface morphology and wear track profiles show that pronounced plow-like wear tracks are observable on the coating surfaces under all three hydrostatic pressure conditions and amplify in quantity with increasing hydrostatic pressure. The depth of these furrows remains at approximately 100 nm and does not significantly change with increasing hydrostatic pressure. Based on the cross-sectional structure of the coatings in Fig. 2, it is evident that the depth of these grooves does not exceed the thickness of the coating, indicating that localized wear occurs only on a small portion of the coating surface. Additionally, upon examination of the surface morphology and corresponding cross-sectional profiles in the areas adjacent to the wear grooves, as shown in Figs. 7(d) and 7(c) (highlighted by blue circles), it is apparent that these areas have not suffered significant wear and still retain the surface characteristics of the original coating, as shown in Fig. 4(a). During the friction process, the entire surface does not come into complete contact owing to microscale waviness at the friction interface, and distinct regions of solid–solid contact and water lubrication coexist within the interface. These two regions are relatively altered by different hydrostatic pressure conditions, subsequently influencing the tribological performance.

Figure 8 shows the microscopic surface morphology of the coating and energy dispersive analysis under 30 MPa hydrostatic pressure to elucidate the wear mechanisms of the Cr/GLC multilayered coating. The wear track displayed in the figure presents a width of approximately 23 μm, and its bottom section exhibits a shallow depth without indications of cracking or delamination. Numerous cracks are visible on both sides of the edges of the scuff marks, but the remaining area retains significant features of the as-deposited coating. The nodular defects on the bottom of the wear track have gradually smoothed out due to friction, and in some sections, they reveal the structural features of the multilayered coating after wear. During the process of friction, the counter-surface initially comes into contact with these raised nodular defects, which are then worn down. The defects have weak bonding with the surrounding matrix, which is evident through the presence of cracks in the matrix (Fig. 2(c)), making them susceptible to stress concentration under the influence of frictional shear forces. As a result, these defects may act as potential risk zones for coating delamination. The EDS results at the defect site (Fig. 8(c)) show a significant enrichment of elements other than the intrinsic constituents of the coating. Apart from the native coating elements, there is a notable increase in oxygen (O) and silicon (Si) contents. The accumulation of O element suggests that the intermediate Cr layer exposed during the friction process is gradually oxidized. The enrichment of nitrogen (N) is related to the frictional chemical reactions of Si_3N_4 ceramics in the water environment. These chemical reactions

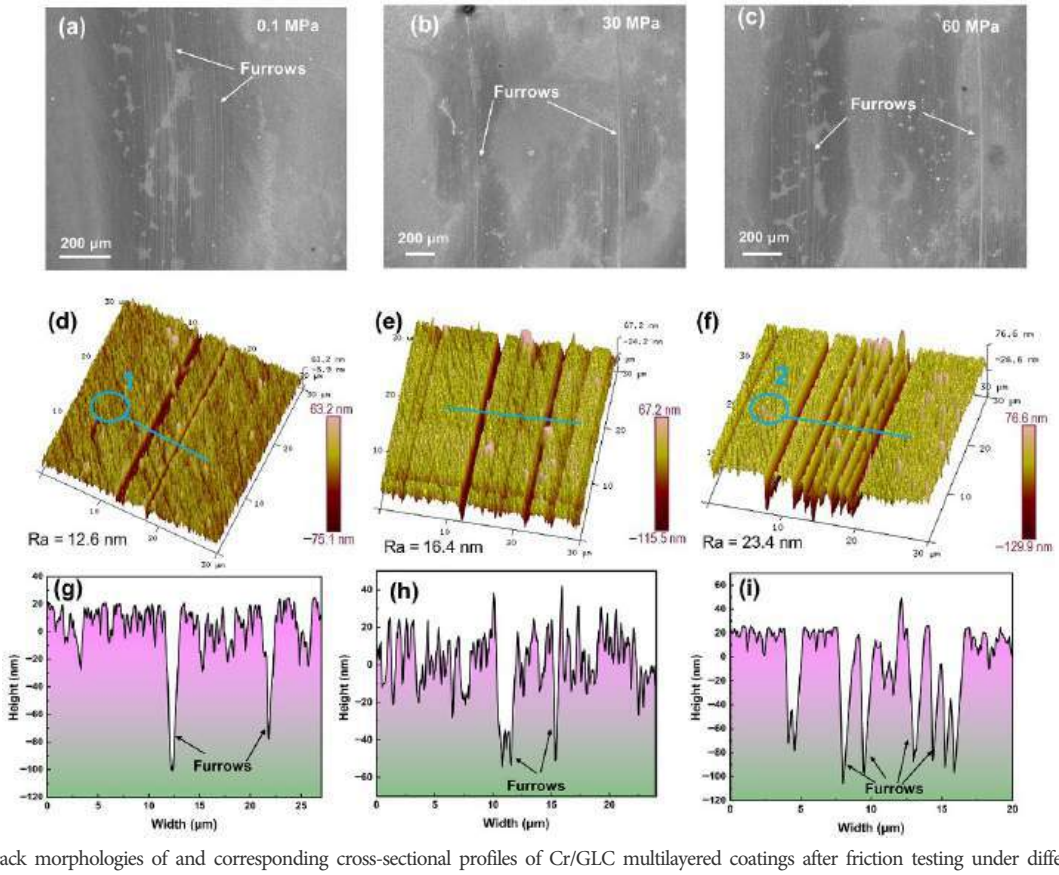

Fig. 7 Wear track morphologies of and corresponding cross-sectional profiles of Cr/GLC multilayered coatings after friction testing under different hydrostatic pressures when the applied load keeps constant at 500 N: (a, d, g) 0.1 MPa, (b, e, h) 30 MPa, and (c, f, i) 60 MPa.

清華大学出版社 Tsinghua University Press | SciOpen

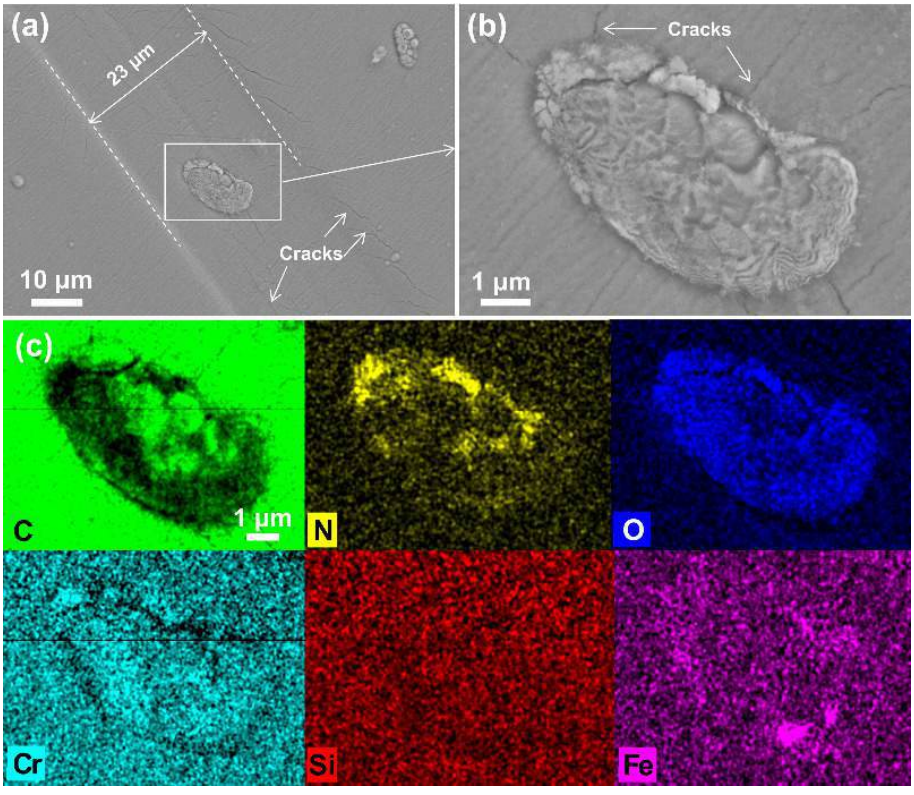

Fig. 8 (a) Wear track morphologies of Cr/GLC multilayered coating after friction test at 30 MPa and (b) nodular-like defects; (c) corresponding EDS mapping results.

create Si-based lubricants that aid in reducing friction between the friction pair [36]. From the analysis of the friction morphology, it can be inferred that localized projections on the harder Si_3N_4 ceramic surface come into solid–solid contact with the softer GLC coating, resulting in local plastic deformation within the GLC coating. In addition, owing to the inherently unstable nature of the nodular defects, the defects protrude and contact the Si_3N_4 ceramic surface initially and act as crack initiation sites.

Figure 9 shows the morphology and EDS results for the crater-like defects on the surface of the Cr/GLC multilayered coating under 30 MPa. The depiction displays a significant presence of white frictional debris inside the defects, which confirms that this section is mainly composed of silicon-based wear debris. Although there is an evident increase in iron (Fe) content, this enrichment is likely a result of defects' insufficient shielding capacity from the substrate rather than delamination of the coating. The coating surface around the defects exhibits the typical morphology of the as-deposited coating, indicating that this region was in a state of liquid lubrication during the friction process. Previous research has demonstrated that texturing the surface of amorphous carbon coatings can trap wear debris and lubricants, which has a positive effect on improving the tribological performance of friction pairs. As a result, crater-like defects found in the Cr/GLC multilayered coating may act as reservoirs during the friction process, store wear debris and lubricants, and thus enhance the tribological performance through surface texturing.

The aforementioned tribological morphology analysis indicates the presence of distinct solid–solid contact regions and water lubrication regions within the friction interface during the friction process. The performance of the friction pair results from the synergistic interaction between these two lubrication mechanisms. Changes in hydrostatic pressure alter the tribological performance by influencing the collaborative effect of these two lubrication mechanisms. The growth defects within the Cr/GLC multilayered coating may play a dual role, either by improving the lubrication state or serving as initiation sites for coating cracks, thereby becoming potential weak points.

3.3.2 Wear morphologies under different applied load forces

Figure 10 shows the surface morphology and EDS mapping results of the Cr/GLC multilayered coating under a hydrostatic pressure of 30 MPa and a load of 1,000 N. In addition to the noticeable abrasions on the surface of the coating, the localized magnified view (Fig. 10(b)) shows the absence of the as-deposited surface structure, indicating a pronounced smoothing effect induced by friction. The EDS mapping of the entire friction interface shows a uniform distribution of surface elements, indicating excellent surface contact during the friction process, resulting in the formation of a full solid–solid contact area. The aforementioned features of the friction morphology suggest that with increasing applied force (contact pressure of 2.92 MPa), the solid–solid contact area within the friction interface gradually increases.

As the applied load increases to 1,500 N (Fig. 11), the surface of the Cr/GLC multilayered coating exhibits more pronounced nodular-like defects. The raised nodular defects gradually flatten, exposing the underlying multilayered structure. The EDS results reveal a pronounced enrichment of Cr and O elements. This occurrence is attributed to the friction-induced wear of the upper GLC coating layer, which exposes the underlying Cr interlayer. Consequently, this exposure leads to frictional oxidation and electrochemical corrosion processes. The 3D surface topography images provide a visual representation of the process by which the increase in load results in the smoothing of the friction surface. Figure 12 displays the friction surface and its cross-section under a 1,500 N load. Cross-sectional images at the positions marked by the blue lines in the 3D surface topography (Figs. 12(b) and 12(c)) show that the surface roughness on both sides of the abrasions is lower than that of the original as-deposited coating, indicating that

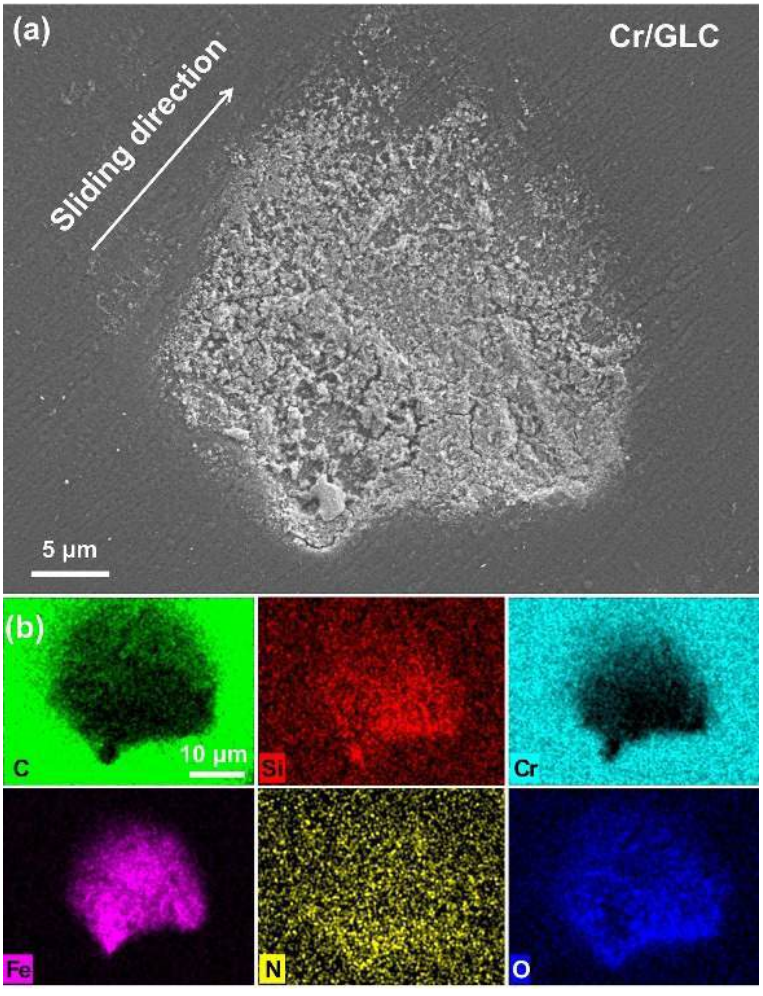

Fig. 9 (a) Wear track morphologies of Cr/GLC multilayered coating at penetrating defects after friction test under 30 MPa and (b) corresponding EDS mapping results.

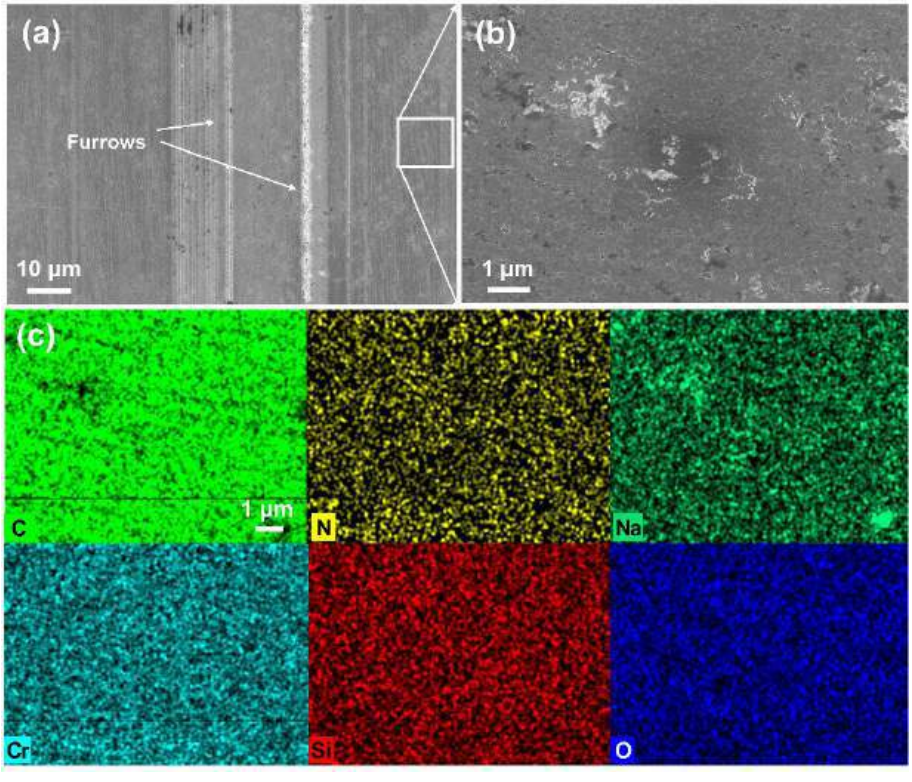

Fig. 10 (a, b) Wear morphologies of Cr/GLC multilayered coating after friction test when applied load keeps constant at 1,000 N and (c) corresponding EDS mapping results of (b).

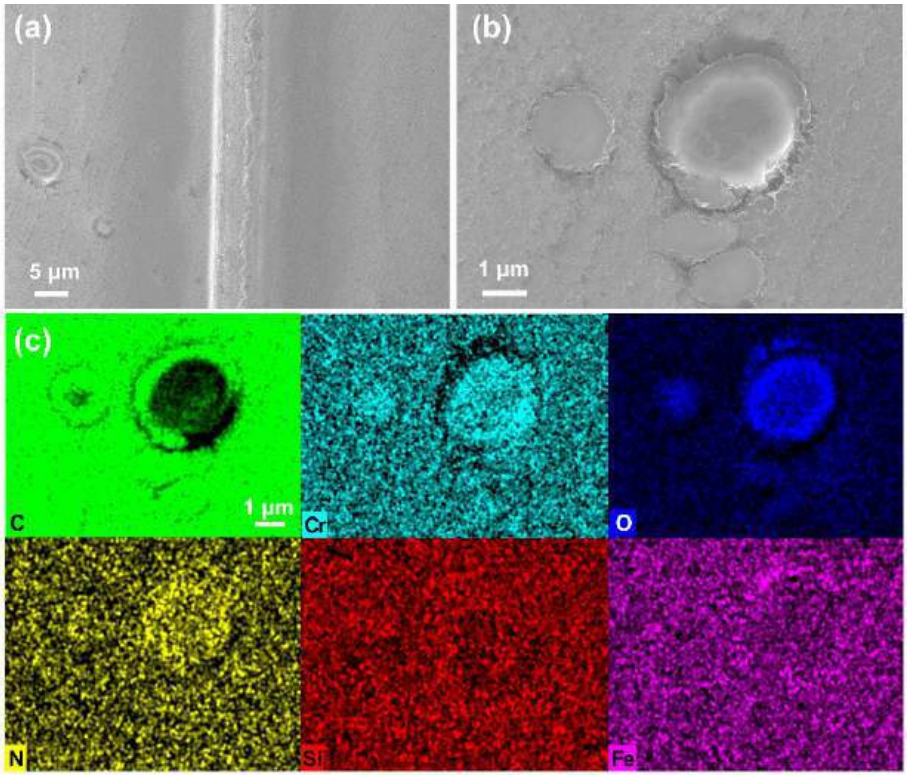

Fig. 11 (a, b) Wear morphologies of Cr/GLC multilayered coating after friction test when applied load keeps constant at 1,500 N and (c) corresponding EDS mapping results of (b).

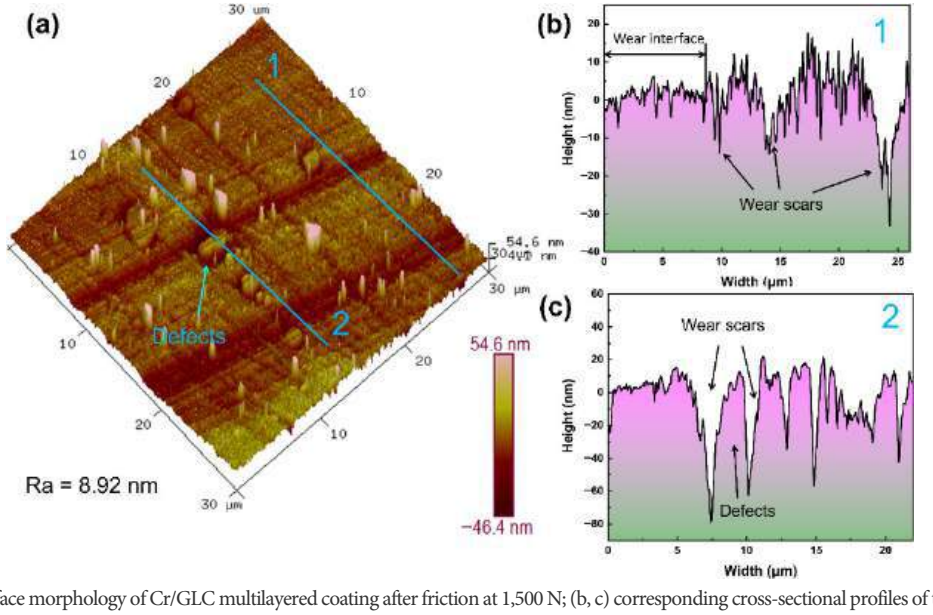

Fig. 12 (a) 3D wear surface morphology of Cr/GLC multilayered coating after friction at 1,500 N; (b, c) corresponding cross-sectional profiles of the two blue lines in (a).

these areas have become smoother and more uniform because of friction.

The changes in morphology observed above indicate that increasing contact load significantly increases the solid–solid contact area within the friction interface under constant hydrostatic pressure conditions. As the load increases from 500 to 1,500 N, the contact stress between the friction pair increases correspondingly from 1.96 to 5.88 MPa. Under the influence of this contact stress, the hard particles present on the surface of the Si_3N_4 friction ring are ploughed and removed from the relatively softer surface of the GLC coating. As a result, the surface exhibits both deep grooves and smooth solid–solid contact areas. The increased load brings the geometric profiles of friction-pairing surfaces closer together, resulting in an increase in solid–solid contact and a gradual reduction in the role of water lubrication. The presence of a graphitized transfer film in the solid–solid contact area serves as its lubrication mechanism, and the presence and distribution of this transfer film significantly affect the performance of the friction pair. In this study, the increase in load results in an increase in the coefficient of friction, which is associated with the uneven formation and distribution of the transfer film.

Figure 13 shows the post-wear morphology and EDS results of the Si_3N_4 friction ring under different test conditions. As shown in

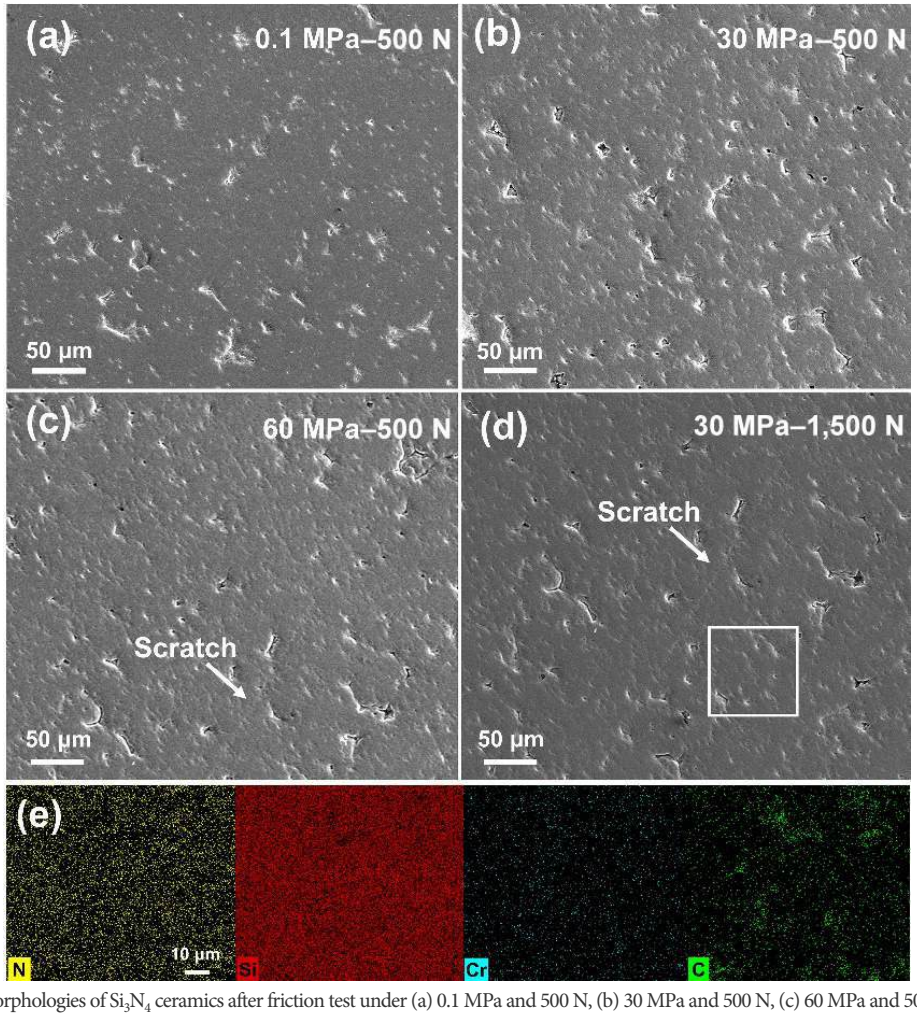

Fig. 13 Wear surface morphologies of Si_3N_4 ceramics after friction test under (a) 0.1 MPa and 500 N, (b) 30 MPa and 500 N, (c) 60 MPa and 500 N, and (e) 30 MPa and 1,500 N; (e) EDS mapping results for square area in (d).

the figures, the friction surface of the Si_3N_4 friction ring exhibits consistent characteristics regardless of variations in the hydrostatic pressure or contact load. These characteristics include typical pit-like defects, localized scratches, and carbon enrichment within the defects, which are particularly evident under conditions of 30 MPa and 1,500 N loading, as shown in Fig. 13(e). This minimal wear can be attributed to the superior mechanical properties of Si_3N_4 material.

3.4 Raman spectral analysis

Raman spectroscopy was employed to analyze the carbon bonding structure of the Cr/GLC coatings and Si_3N_4 ceramics before and after friction under different experimental conditions, as shown in Fig. 14. Figure 14(a) presents the Raman spectroscopy results of the multilayered Cr/GLC coatings after friction in different hydrostatic pressure environments. A comparison of these results with those of the as-deposited coating samples clearly reveals that after friction, these Cr/GLC coating surfaces still exhibit a prominent D peak and a relatively weaker G peak. No distinct intensity peaks are visible in the spectra of the Cr/GLC multilayered coating after friction. Instead, two widened peaks are consistently detectable in the range of 900–1,800 cm^{-1}, implying that after friction, the surface still preserves a graphite-like structure. The presence of the D peak is attributed to the disorder in the sp^2 hybridized bond angles, and a stronger D peak indicates a higher content of sp^2 hybridized bonds within the carbon coatings [37]. The Raman spectra underwent peak fitting through two Gaussian curves, and the outcomes for the intensity ratio of D peak to G peak (I_D/I_G), peak positions, and half-widths are displayed in Fig. 14(b). It is clear that the I_D/I_G values on the surface of the Cr/GLC multilayered coating after friction under different hydrostatic pressure conditions are significantly greater than those of the as-deposited coatings. At 15 MPa, the maximum value of 3.02 is reached. For the hydrogen-free GLC coatings, a higher value of I_D/I_G represents a greater content of sp^2 hybridized bonds. The position of the G peak shifts towards higher wavenumbers as the hydrostatic pressure increases. It ranges from 1,550.57 cm^{-1} in the as-deposited state to 1,553.26 cm^{-1} at 60 MPa, but the shift is not linearly related to hydraulic pressure. The half-width of the G peak (G_{FWHM}) decreases as the hydrostatic pressure increases.

Moreover, the surface Raman spectra of the multilayered Cr/GLC coating samples subjected to friction experiments under varying applied loads demonstrate consistent tendencies (Figs. 14(c) and 14(d)). Notably, there is an increase in I_D/I_G and the G peak position with increasing applied load, whereas the G_{FWHM} decreases with increasing load. The observed variations imply that modifying the hydrostatic pressure or employing diverse loads leads to an elevated concentration of sp^2 hybridized bonds on the GLC coating surface. This means that both hydrostatic pressure and load induce a significant surface graphitization transformation during the friction process. The Raman spectroscopic results of the Si_3N_4 ceramic surface after friction testing indicate two different peaks. One peak is stronger

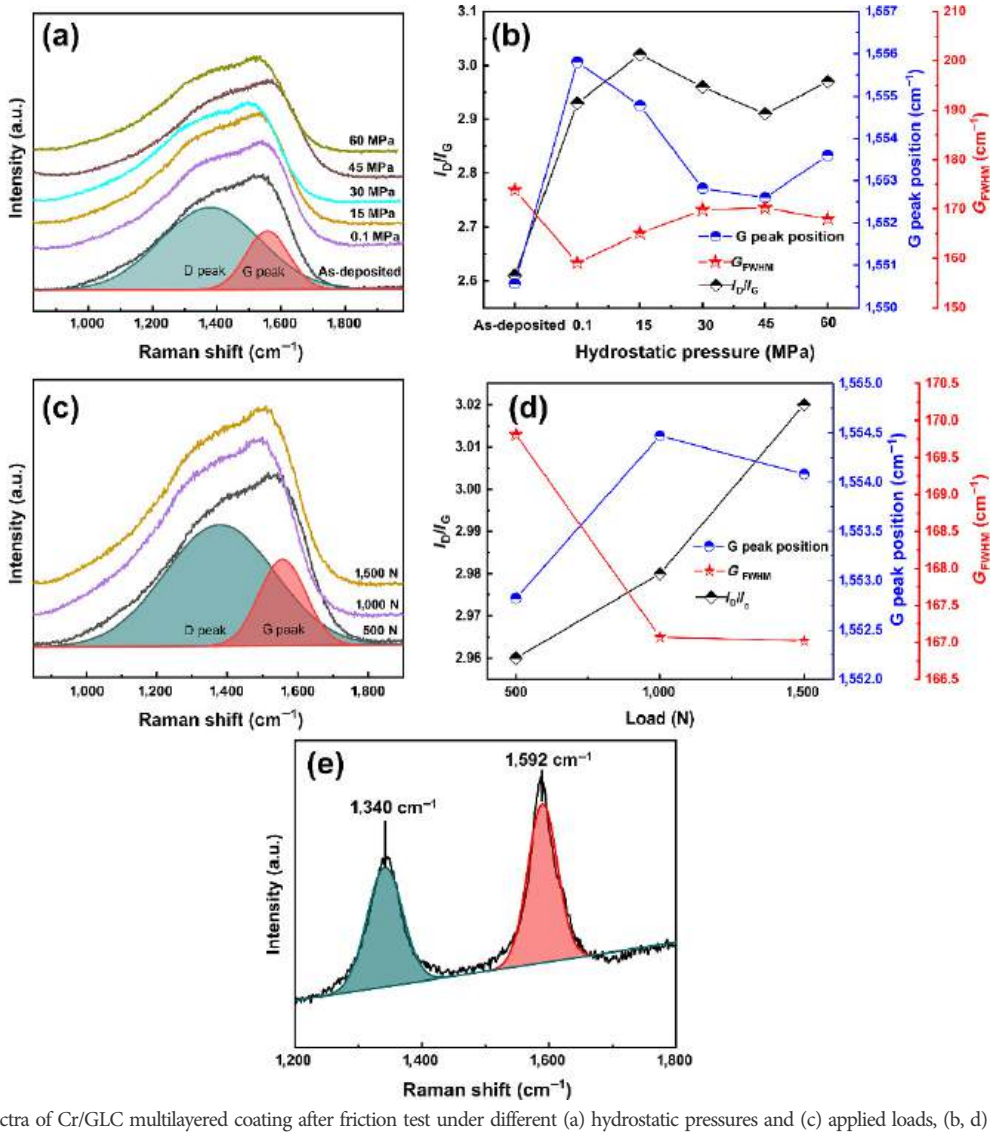

Fig. 14 Raman spectra of Cr/GLC multilayered coating after friction test under different (a) hydrostatic pressures and (c) applied loads, (b, d) corresponding fitted results of I_D/I_G, $G_{position}$, and G_{FWHM}, (e) Raman spectra of Si_3N_4 ceramics after friction under loads of 500 N and 0.1 MPa.

at 1,592 cm^{-1} and the other is weaker at 1,340 cm^{-1}; these peaks closely resemble the graphite peaks [38]. The results suggest the presence of a significant amount of crystalline graphitized transfer film during the friction process. This film plays a key role in providing effective solid lubrication for the friction surface.

4 Discussion

4.1 Effect of hydrostatic pressure on contact stress of friction pair

Under challenging conditions in deep-sea environments, hydrostatic pressure, a pivotal environmental factor, profoundly shapes the performance of friction materials. Previous studies, particularly those focused on polymers, have explored primarily the effects of hydrostatic pressure, centering on two key aspects. On one hand, the hydrostatic pressure affects the water absorption characteristics of polymeric materials, which subsequently leads to changes in their mechanical properties, ultimately resulting in deterioration of their frictional properties [39]. On the other hand, within the hydrostatic pressure range set in this study (0.1–60 MPa), the variation in seawater viscosity does not exceed 4%, and thus its effect on the performance of friction pairs can be neglected [40]. Compared with those of polymeric materials, the mechanical properties of the mating friction materials in this study, such as 17-4PH stainless steel, Cr/GLC multilayered coatings, and Si_3N_4 ceramics, are not degraded by water penetration and absorption. Consequently, hydrostatic pressure, like applied loads, affects the frictional performance by changing the contact stress conditions during the frictional process.

In this study, a high-pressure friction wear tester, as shown in Fig. 15(a), was used to conduct the experiments. Inside the high-pressure valve, artificial seawater at various hydrostatic pressures is injected by an external high-pressure plunger pump to facilitate friction experiments. Consequently, under certain hydrostatic pressure conditions, the force distribution within the friction pair is represented by the arrows in the figure. It is clear that in the normal direction, in addition to the applied load, the friction pair also experiences an additional load, F_A, induced by the hydrostatic pressure. Therefore, the hydrostatic pressure causes changes in the actual contact stress between the friction pair, and these changes are related to the actual contact area at the friction interface.

Assuming that at a hydrostatic pressure of P, the actual contact force F_N between the friction pair is composed of two parts: the applied force F and the additional force F_A induced by the hydrostatic pressure, i.e.,

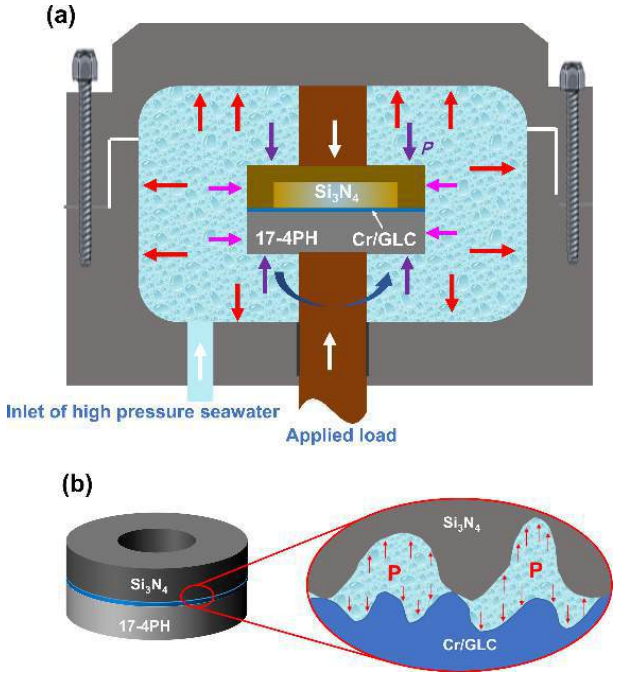

Fig. 15 (a) Schematic diagram of hydrostatic pressure distribution inside autoclave and (b) contact surface.

$$F_N = F + F_A \tag{1}$$

The additional load F_A can be further expressed as

$$F_A = P \times S_A \tag{2}$$

where S_A represents the actual contact area of the friction surface under the hydrostatic pressure P. Combining Eqs. (1) and (2), the actual contact load at a hydro pressure of P can be defined as

$$F_N = F + P \times S_A \tag{3}$$

Obviously, the actual area S_A is also influenced by the hydrostatic pressure and the contact conditions of the friction interface, such as surface roughness. The normal additional load induced by hydrostatic pressure affects the friction pair, while liquid diffusion also occurs in the gaps of the friction contact surface due to hydrostatic pressure. This phenomenon influences the lubrication status of the friction interface. Based on the analysis of the surface morphology of the coatings and Si_3N_4 ceramics, it is clear that the surfaces of the friction pair have many microscopic protrusions. As a result, the friction interface is not an area of complete solid-to-solid contact. Figure 15(b) displays a schematic diagram of the friction interface, indicating the existence of numerous small gaps at the microscale. The diffusion and infiltration of water into gaps are accelerated by hydrostatic pressure, thereby altering the contact area and lubrication state at the friction interface. The magnitude of this area is a critical factor influencing the frictional process. In the absence of interfacial friction chemistry, frictional force may be conceptualized as the disruption of bonds occurring at microscale junctions between contacting surfaces. Consequently, the fracture strength and resulting frictional force are expected to be proportional to the actual contact area. Consequently, under increasing contact loads and higher hydrostatic pressure conditions, there is a corresponding rise in the lateral shear resistance of microscale protrusions at the friction interface, leading to elevated friction coefficients. At a hydrostatic pressure of 45 MPa, the additional load induced by the hydrostatic pressure leads to an increase in the actual contact stress between the frictional contact surfaces, which in turn causes an expansion of the solid–solid contact area between the friction pairs. Consequently, the area of the corresponding liquid-lubricated region decreases. Since, at this point, the hydrostatic pressure is unable to further promote the diffusion of liquid through the pores, the improvement in the lubrication state of the interface caused by the hydrostatic pressure is relatively less pronounced. In this scenario, we suggest that at 45 MPa, the discrepancy between the effects of increased additional load and improved interface lubrication is at its greatest, resulting in the highest coefficient of friction observed at this pressure. The gradual wear and fracturing of microscale protrusions cause fluctuations in the friction coefficient during the friction process. With continued friction, the interface smoothens, and the presence of a graphite transfer film gradually reduces the friction coefficient. In summary, the effect of hydrostatic pressure on the friction process is essentially achieved by changing the contact area of the friction pair, neglecting variations in seawater viscosity and changes in the friction materials themselves. As the hydrostatic pressure increases, the actual contact area and mode between the friction pair change and ultimately affect the performance of the friction pair.

4.2 Tribological mechanism of the Cr/GLC-Si_3N_4 friction pair under hydrostatic pressure

The anti-wear lubrication properties of GLC coatings are due to their relatively high carbon content in the form of a graphite-like structure and their low environmental sensitivity. Given the presence of numerous microscopic surface irregularities on the friction pairing materials, combined with the low viscosity characteristics of water, it is evident that in the process of water-lubricated friction, the microscale friction interface inevitably contains both a solid–solid contact zone and a liquid lubrication zone. Thus, under hydrostatic pressure, the friction state of the friction pair is a hybrid friction mechanism in which both solid-to-solid contact and water lubrication zones coexist.

In the solid–solid contact region, the friction properties of the friction couple are comparable to those in dry friction situations. The self-lubrication of graphite-like carbon structures results in lower friction coefficients for the friction pair. Hydrostatic pressure affects frictional performance by changing the actual contact area, and its effect is comparable to that of applied loads. Increasing the hydrostatic pressure accelerates surface abrasion and smoothing on the friction surface, resulting in the formation of a more completely lubricating transfer film. This leads to a continuous increase in the area of solid–solid contact. During the early stages of friction, the fluctuations observed in the friction curve are attributed to the constant breaking of micro-scale protrusions at the friction interface. The initial state of the friction interface leads to rapid variations in the COF. As friction continues, the rate of interface smoothing gradually decreases, culminating in a stable state with a constant COF. The results of Raman spectroscopy, surface morphology analysis, and EDS mapping confirm the friction characteristics and their evolution in the solid–solid contact zone, providing clear evidence of the frictional properties and their changes.

In the water lubrication zone, the lubrication properties of the interface are affected by the distributions of transfer films, graphite debris, and silicon-based friction products. Owing to the lubrication properties of water and the self-lubricating features of graphite debris, hydrostatic pressure has the ability to hasten particular processes. On one hand, water diffusion and filling into microscopic gaps at the friction interface accelerate due to

hydrostatic pressure, ultimately increasing the area and thickness of the water lubrication zone. On the other hand, the additional load F_A caused by hydrostatic pressure enlarges the friction contact area. Consequently, the presence of the water lubrication zone is gradually reduced as the interface smoothing process takes place. The friction mechanism shifts to solid-to-solid contact with a graphite transfer film.

Additionally, Si_3N_4 ceramics experience frictional chemical reactions in aqueous solutions when exposed to shear forces:

$$Si_3N_4 + 6H_2O = 3SiO_2 + 5NH_3 \quad (4)$$

$$3SiO_2 + 2H_2O = Si(OH)_4 \quad (5)$$

The resulting products, $Si(OH)_4$ or $Si_x(OH)_y$, display exceptional lubricating abilities. Surface EDS mapping analysis after friction experiments confirms the existence of these products.

Hence, in this study, hydrostatic pressure effectively altered the contact stress and interface lubrication state of the friction pair samples. The combined impact of these two factors ultimately influences the performance of the friction pair. In environments with higher hydrostatic pressure, the increase in contact stress induced by additional loads hastens the levelling process of the friction interface. Moreover, it accelerates the generation and formation of graphitized transfer films and silicon-based lubrication products. The presence of a visible graphite transfer film and reaction products containing silicon on the friction surface additionally aids in facilitating lubrication at the interface. Given the constrained timeframe of the friction experiment and the effective lubrication at the interface under the hydrostatic pressure condition, the wear mass loss of the sample proves negligible, rendering the acquisition of meaningful wear data unfeasible. Consequently, discussion pertaining to wear rate was not conducted in the present study.

5 Conclusions

This study investigated the frictional behavior of Cr/GLC coatings in conjunction with their Si_3N_4 counterparts subjected to different hydrostatic pressures and loads sing a simulated deep-sea friction and wear test system. The analysis of the influence mechanism of hydrostatic pressure on the tribological properties of Cr/GLC multilayered coatings was conducted by investigating the friction surface morphology and Raman spectroscopy. These findings suggest that the effect of hydrostatic pressure on the frictional performance of GLC coatings is achieved by changing the state of the frictional contact surfaces. In principle, the hydrostatic pressure modifies the real contact area (S_F) of the friction pair by generating additional compressive loads such that an increase in hydrostatic pressure has a similar effect on the increase in applied load. As the hydrostatic pressure and applied load increase, the trend of abrasion smoothing on the surfaces of the friction pair becomes more pronounced. The presence of distinct graphitic transfer films and silicon-based reaction products on friction surfaces functions as a lubrication mechanism in the region of solid–solid contact.

Acknowledgements

This work was financially supported by the National Key R&D Program of China (No. 2022YFC2805701), the National Science Fund for Distinguished Young Scholars of China (No. 52025014), the National Natural Science Foundation of China (No. 52127803), and the Ningbo Science and Technology Innovation Project (No. 2023Z198).

CRediT authorship contribution statement

Yingrui Liu: methodology investigation, validation, and writing original article; Xiaohui Zhou: visualization; Peng Guo: methodology investigation, writing, review, and editing; Yinshui Liu: methodology investigation; Jing Wei: methodology investigation; Wei Yang: methodology investigation; Kazuhito Nishimura: writing, review, editing, and funding acquisition; Aiying Wang: writing, review, and editing, funding acquisition, and supervision. Peiling Ke: writing, review, and editing, supervision, and funding acquisition. All the authors discussed the results and commented on the manuscript.

Declaration of competing interest

The authors have no competing interests to declare that are relevant to the content of this article.

References

[1] Field S K, Jarratt M, Teer D G. Tribological properties of graphite-like and diamond-like carbon coatings. *Tribol Int* **37**: 949–956 (2004)
[2] Tillmann W, Lopes Dias N F, Stangier D. Tribo-mechanical properties of CrC/a-C thin films sequentially deposited by HiPIMS and mfMS. *Surf Coat Tech* **335**: 173–180 (2018)
[3] Li L, Guo P, Liu L L, Li X W, Ke P L, Wang A Y. Structural design of Cr/GLC films for high tribological performance in artificial seawater: Cr/GLC ratio and multilayer structure. *J Mater Sci Technol* **34**(8): 1273–1280 (2018)
[4] Khamseh S, Alibakhshi E, Ramezanzadeh B, Sari M G, Nezhad A K. Developing a graphite like carbon: Niobium thin film on GTD-450 stainless steel substrate. *Appl Surf Sci* **511**: 145613 (2020)
[5] Wang Y X, Wang L P, Li J L, Chen J M, Xue Q J. Tribological properties of graphite-like carbon coatings coupling with different metals in ambient air and water. *Tribol Int* **60**: 147–155 (2013)
[6] Wang Y X, Wang L P, Wang S C, Zhang G G, Wood R J K, Xue Q J. Nanocomposite microstructure and environment self-adapted tribological properties of highly hard graphite-like film. *Tribol Lett* **40**(3): 301–310 (2010)
[7] Wang Y X, Wang L P, Xue Q J. Controlling wear failure of graphite-like carbon film in aqueous environment: Two feasible approaches. *Appl Surf Sci* **257**(9): 4370–4376 (2011)
[8] Wang L P, Guan X Y, Zhang G G. Friction and wear behaviors of carbon-based multilayer coatings sliding against different rubbers in water environment. *Tribol Int* **64**: 69–77 (2013)
[9] Li Z C, Guan X Y, Wang Y X, Li J L, Cheng X Y, Lu X, Wang L P, Xue Q J. Comparative study on the load carrying capacities of DLC, GLC and CrN coatings under sliding-friction condition in different environments. *Surf Coat Tech* **321**: 350–357 (2017)
[10] Wang Y X, Li J L, Shan L, Chen J M, Xue Q J. Tribological performances of the graphite-like carbon films deposited with different target powers in ambient air and distilled water. *Tribol Int* **73**: 17–24 (2014)
[11] Wang Y X, Wang L P, Zhang G G, Wang S C, Wood R J K, Xue Q J. Effect of bias voltage on microstructure and properties of Ti-doped graphite-like carbon films synthesized by magnetron sputtering. *Surf Coat Tech* **205**(3): 793–800 (2010)
[12] Guan X Y, Wang Y X, Wang J F, Xue Q J. Adaptive capacities of chromium doped graphite-like carbon films in aggressive solutions with variable pH. *Tribol Int* **96**: 307–316 (2016)
[13] Liu X Q, He X, Lin Y F, Zhuang J W, Hao J Y. Enhanced adhesion strength and solid lubricity of graphite like amorphous carbon films by hydrogen implantation. *Surf Coat Tech* **412**: 127013 (2021)
[14] Li L, Liu L L, Li X W, Guo P, Ke P L, Wang A Y. Enhanced tribocorrosion performance of Cr/GLC multilayered films for marine protective application. *ACS Appl Mater Inter* **10**(15): 13187–13198 (2018)
[15] Guan X Y, Lu Z B, Wang L P. Achieving high tribological performance of graphite-like carbon coatings on Ti_6Al_4V in aqueous

environments by gradient interface design. *Tribol Lett* **44**(3): 315 (2011)
[16] Liu Y R, Li S Y, Li H, Ma G S, Sun L L, Guo P, Ke P L, Lee K R, Wang A Y. Controllable defect engineering to enhance the corrosion resistance of Cr/GLC multilayered coating for deep-sea applications. *Corros Sci* **199**: 110175 (2022)
[17] Liu Y R, Du H, Zuo X, Guo P, Liu L, Lee K R, Wang A Y, Ke P L. Cr/GLC multilayered coating in simulated deep-sea environment: Corrosion behavior and growth defect evolution. *Corros Sci* **188**: 109528 (2021)
[18] Wang J Z, Chen J, Chen B B, Yan F Y, Xue Q J. Wear behaviors and wear mechanisms of several alloys under simulated deep-sea environment covering seawater hydrostatic pressure. *Tribol Int* **56**: 38–46 (2012)
[19] Wang J Z, Yan F Y, Xue Q J. Tribological behavior of PTFE sliding against steel in sea water. *Wear* **267**(9–10): 1634–1641 (2009)
[20] Liu H, Wang J, Jiang P, Yan F Y. Accelerated degradation of polyetheretherketone and its composites in the deep sea. *R Soc Open Sci* **5**(4): 171775 (2018)
[21] Liu H, Wang J Z, Jiang P F, Yan F Y. Hydrostatic pressure-dependent wear behavior of thermoplastic polymers in deep sea. *Polym Adv Technol* **29**(8): 2410–2415 (2018)
[22] Wu D F, Guan Z W, Cheng Q, Guo W, Tang M, Liu Y S. Development of a friction test apparatus for simulating the ultra-high pressure environment of the deep ocean. *Wear* **452**: 203294 (2020)
[23] Li S Y, Li H, Ma G S, Wei J, Zhou G X, Zhang Y, Guo P, Ke P L, Wang A Y. Dense Cr/GLC multilayer coating by HiPIMS technique in high hydrostatic pressure: Microstrusctural evolution and galvanic corrosion failure. *Corros Sci* **225**: 111618 (2023)
[24] Liu Y R, Li S Y, Zhou X H, Guo P, Chen R D, Wei J, Wang A Y, Ke P L. Enhanced anti-tribocorrosion property of a-C film under high hydrostatic pressure by high power pulsed magnetron sputter (HiPIMS). *J Mater Res Technol* **28**: 3052–3067 (2024)
[25] Li H, Liu L L, Guo P, Sun L L, Wei J, Liu Y R, Li S Y, Wang S Y, Lee K R, Ke P L, et al. Long-term tribocorrosion resistance and failure tolerance of multilayer carbon-based coatings. *Friction* **10**(10): 1707–1721 (2022)
[26] Hoffmann M J, Petzow G. Tailoring of mechanical properties of Si_3N_4 ceramics. Dordrech (the Netherlands): Springer Science & Business Media, 2012.
[27] Wu D F, Cheng Q, Yu Q, Guan Z W, Deng Y P, Liu Y S. Influence of high hydrostatic pressure on tribocorrosion behavior of HVOF WC–10Co–4Cr coating coupled with Si_3N_4 in artificial seawater. *Int J Refract Met H* **108**: 105936 (2022)
[28] Guan Z W, Wu D F, Cheng Q, Wang Z Y, Tang M, Liu Y S. Friction and wear characteristics of CF/PEEK against 431 stainless steel under high hydrostatic pressure water lubrication. *Mater Des* **196**: 109057 (2020)
[29] Davis C A, Amaratunga G A J, Knowles K M. Growth mechanism and cross-sectional structure of tetrahedral amorphous carbon thin films. *Phys Rev Lett* **80**(15): 3280–3283 (1998)
[30] Robertson J, O'Reilly E P. Electronic and atomic structure of amorphous carbon. *Phys Rev B Condens Matter* **35**(6): 2946–2957 (1987)
[31] Drnovšek A, Panjan P, Panjan M, Čekada M. The influence of growth defects in sputter-deposited TiAlN hard coatings on their tribological behavior. *Surf Coat Tech* **288**: 171–178 (2016)
[32] Panjan P, Drnovšek A, Gselman P, Čekada M, Panjan M, Bončina T, Kek Merl D. Influence of growth defects on the corrosion resistance of sputter-deposited TiAlN hard coatings. *Coatings* **9**(8): 511 (2019)
[33] Panjan P, Gselman P, Kek-Merl D, Čekada M, Panjan M, Dražić G, Bončina T, Zupanič F. Growth defect density in PVD hard coatings prepared by different deposition techniques. *Surf Coat Tech* **237**: 349–356 (2013)
[34] Tait R N, Smy T, Dew S K, Brett M J. Nodular defect growth and structure in vapor deposited films. *J Electron Mater* **24**: 935–940 (1995)
[35] Wang Y, Hadfield M. Failure modes of ceramic rolling elements with surface crack defects. *Wear* **256**: 208–219 (2004)
[36] Huang L, Dai Q W, Huang W, Wang X L. Ni/Si_3N_4 composite coatings and their water lubrication behaviors. *Appl Surf Sci* **572**: 151534 (2022)
[37] Modabberasl A, Kameli P, Ranjbar M, Salamati H, Ashiri R. Fabrication of DLC thin films with improved diamond-like carbon character by the application of external magnetic field. *Carbon* **94**: 485–493 (2015)
[38] Sui X D, Liu J Y, Zhang S T, Yang J, Hao J Y. Microstructure, mechanical and tribological characterization of CrN/DLC/Cr-DLC multilayer coating with improved adhesive wear resistance. *Appl Surf Sci* **439**: 24–32 (2018)
[39] Liu H, Wang J Z, Jiang P F, Yan F Y. Hydrostatic pressure-dependent corrosion behaviour of polytetrafluoroethylene composites in the deep sea. *Corros Sci* **139**: 289–300 (2018)
[40] Schumacher M M. *Seawater Corrosion Handbook*. Park Ridge (USA): Noyes Data Co., 1979.

Yingrui Liu received his Ph.D. degree from University of Chinese Academy of Sciences (CAS) in January 2022. He is currently an associate professor at Chongqing Institute of Green and Intelligent Technology, CAS. His research interests are design and preparation of solid lubricant coating materials and their corrosion-friction-coupled damage behavior in deep-sea environments.

Peiling Ke received her Ph.D. degree from Institute of Metal Research, Chinese Academy of Sciences (CAS) in 2006, and was assigned to the University of Birmingham, UK. After graduation, she served as a visiting research fellow at the University of Birmingham. Since 2009, she started working at Ningbo Institute of Materials Technology and Engineering (NIMTE), CAS, and has been a professor since 2015. She is currently the director of Public Technology Center of NIMTE. Her research is focused mainly on the use of protective coating materials for marine applications and related evaluation methodologies.